European Society of Computational Methods in Sciences and Engineering (ESCMSE)

Journal of Numerical Analysis, Industrial and Applied Mathematics (JNAIAM)
vol. 3, no. 3-4, 2008, pp. 231-247
ISSN 1790–8140

Prediction of the Flow Around a Short Wall-Mounted Finite Cylinder using LES and DES[1]

O. Frederich[2], E. Wassen & F. Thiele

Institute of Fluid Mechanics and Engineering Acoustics,
Faculty of Mechanical Engineering and Transport Systems,
Berlin University of Technology,
Mueller-Breslau-Str. 8,
10623 Berlin, Germany

Received 30 January 2007; accepted in revised form 20 July 2008

Abstract: Numerical simulations of the turbulent separated flow around a wall-mounted finite cylinder were performed in order to assess the predictive accuracy of the methods for the unsteady flow field at high Reynolds number. While the results obtained from Large-Eddy Simulation show only minor differences to experiments, the Detached-Eddy Simulation exhibits problems in the attached laminar boundary layer. By neglecting this insufficient modelling of the transition phenomenon, the Detached-Eddy Simulation performed can be understood as a Large-Eddy Simulation with an alternative subgrid scale model that delivers qualitatively comparable results to the Large-Eddy Simulation.

Keywords: circular cylinder, wall-mounted, LES, DES, imaging measurements

Mathematics Subject Classification: 76F65

PACS: 47.27.ep

1 Introduction

The three-dimensional and unsteady flow field around a wall-mounted finite circular cylinder is predicted using two different approaches, Large-Eddy Simulation (LES) and the non-zonal hybrid RANS-LES approach of Detached-Eddy Simulation (DES, Spalart *et al.*, 1997) on the same grid. In conjunction with concurrent Laser Doppler Anemometry (LDA, Richter, 2005; Leder, 2003) and Particle Image Velocimetry (PIV, Jensch *et al.*, 2006) experiments, the simulation of this complex flow is intended to provide a combined database and benchmark case for future simulations and experiments. In addition to this main objective, the capability of numerical prediction methods and the influence of the modelling approach are investigated.

The investigations are carried out using a finite circular cylinder with a diameter of $D = 120$ mm and a length-to-diameter ratio of $L/D = 2$. The cylinder is mounted on a ground plate at a

[1]Published electronically October 15, 2008
[2]Corresponding author. E-mail: octavian.frederich@tu-berlin.de

distance of $1.5D$ behind its rounded leading edge (figure 1) to minimise the effect of the boundary layer on the plate, which is tripped by a wire. The Reynolds number based on the diameter is $\mathrm{Re}_D = \frac{U_\infty D}{\nu} = 200,000$, with the inflow velocity U_∞ and the kinematic viscosity ν. The thickness of the approaching boundary layer on the plate has been measured using LDA without the cylinder mounted and is $\delta/D = 0.042$ at $x/D = -0.5$ (the leading edge of the cylinder).

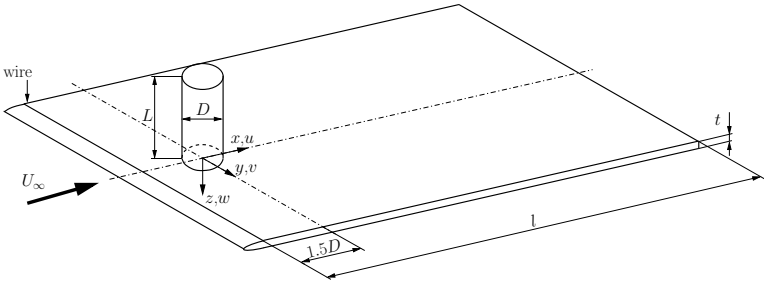

Reynolds number	Re_D	=	$200,000$
Inflow velocity	U_∞	=	26.0m/s
Turbulence level	Tu	=	0.5%
Cylinder diameter	D	=	120mm
Cylinder ratio	L/D	=	2
Plate length	l	=	1300mm

Figure 1: Sketch of the investigated configuration.

The experimental and numerical literature on low aspect ratio finite cylinders is somewhat limited. A comprehensive overview of the measurements conducted for similar cases is given by Pattenden *et al.* (2005), which reveals that there are only few experiments for the present Reynolds number and aspect ratio. In addition, the numerical investigations are mainly concentrated on aspect ratios of 6 and higher as well as lower Reynolds numbers (e.g. Krajnović, 2008, $\mathrm{Re}_D = 20,000$) due to the computational resources required for a testcase inappropriate for RANS. For the present study some relevant investigations have been selected based on comparability, which are summarised with the most important parameters in table 1.

Table 1: Selected investigations used for comparison.

authors	Re_D	L/D	type
Kawamura *et al.* (1984)	$32,000$	2	exp., P, FV
Agui & Andreopoulus (1992)	$220,000$	2	exp., P, FV
Okamoto & Sunabashiri (1992)	$47,000$	2	exp., P, FV
Fröhlich & Rodi (2003)	$43,000$	2.5	num., LES
Leder (2003)	$200,000$	2	exp., LDA
Roh & Park (2003)	$148,000$	1.25	exp., FV
Pattenden *et al.* (2005)	$200,000$	1	exp., P, PIV, FV
Richter (2005)	$200,000$	2	exp., LDA
Jensch *et al.* (2006)	$200,000$	2	exp., TR-PIV
present study	$200,000$	2	num., LES, DES

Additional abbreviations: exp. – experimental, num. – numerical,
P – pressure measurements, FV – flow visualisation,

The flow around the junction formed between a flat plate and an upright wall-mounted cylinder is highly complex and comprises various phenomena, such as a horse shoe vortex, separation, a turbulent wake and transition, as found by Agui & Andreopoulus (1992). The same authors also comment that the instantaneous and time-averaged flow structures differ significantly. Okamoto & Sunabashiri (1992) have shown that there is a strong downwash effect for small

cylinder aspect ratios that forces the flow to reattach to the plate, forming a recirculation region behind the cylinder. KAWAMURA *et al.* (1984) found that the downwash and trailing vortices dominate the vortex shedding pattern and describe how the boundary layer thickness and the aspect ratio influence the flow behaviour. The experimental contributions of PATTENDEN *et al.* (2005) and ROH & PARK (2003) provide topological models for slightly different configurations, the latter being concentrated on the cylinder top. Both demonstrate the complexity of the flow topology investigated and quantify topological details on the cylinder surface.

The numerical investigations of FRÖHLICH & RODI (2003) deliver very important information about different numerical modelling parameters. They clearly demonstrate the necessity of high spatial resolution and report problems with the dynamic subgrid scale model. In addition, the strong influence of the boundary layer thickness, the free stream turbulence level and the blockage are discussed. This aspect underlines the importance of combined numerical and experimental investigations for a particular setup as demonstrated by FREDERICH *et al.* (2007). The results of the experimental partner at the University of Rostock, published in RICHTER (2005), JENSCH *et al.* (2006) and also in LEDER (2003) are therefore primarily employed for comparison.

The numerically predicted field data from the LES and DES approaches are evaluated statistically for quantitative comparison with experimental data. The comparison is based on time-averaged velocities and pressure, Reynolds stresses and RMS values as well as on triple correlations. Such thorough comparison is intended to provide confidence in the numerical results and the findings for the unsteady flow. The extraction of the time-averaged vortical structures assists the understanding of the flow physics and is essential for the investigations of the unsteady flow.

The models and methods used for the numerical flow simulation are summarised in section 2. The results in comparison to experiments and the differences between the flow predictions of LES and DES are discussed in section 3, before a conclusion and an outlook are given.

2 Numerical model and method

The ELAN flow solver of XUE (1998) is used for all numerical simulations, which is under continual development at the authors' institute. ELAN is an implicit solver with a fully conservative 3D-Finite-Volume approximation of the Navier-Stokes equations. The discretisation, which is of second order accuracy in time and space, is semi-block structured and based on general curvilinear coordinates. For the LES the convective terms are approximated by a central differencing scheme of second order blended with five percent of an upwind scheme to provide stability. In the case of DES a hybrid convection scheme with solution-dependent blending of central and upwind based differences is used, taking into account the local velocity gradients (TRAVIN *et al.*, 2002). The continuity equation is conserved by the SIMPLE-algorithm and the decoupling of pressure and velocity is avoided by a Rhie and Chow interpolation (RHIE & CHOW, 1983).

Several turbulence models for RANS calculations and the standard sub-grid scale models for LES are implemented. In addition Detached-Eddy Simulation is implemented for a selection of turbulence models and calibrated against decaying isotropic turbulence.

2.1 Discretisation

The computational domain is bounded by the length of the plate, 10 diameters in the lateral direction and 7 diameters in the vertical direction. The flow field is divided into several blocks with structured grids using a simple domain-decomposition method. In consideration of the three orthogonal sets of walls (plate, cylinder shell and top), a grid with 12.3 million grid points employing hanging nodes was generated (figure 2). The size of the grid cells followed the common practice for LES grids (KRAJNOVIĆ & DAVIDSON, 2004) at the walls and has been estimated to $0.01D$ for the

free-stream flow field using a dissipation spectrum (Pope, 2000). The transition of the boundary layer on the plate is realised by a geometrically modelled wire in order to reflect the experimental setup.

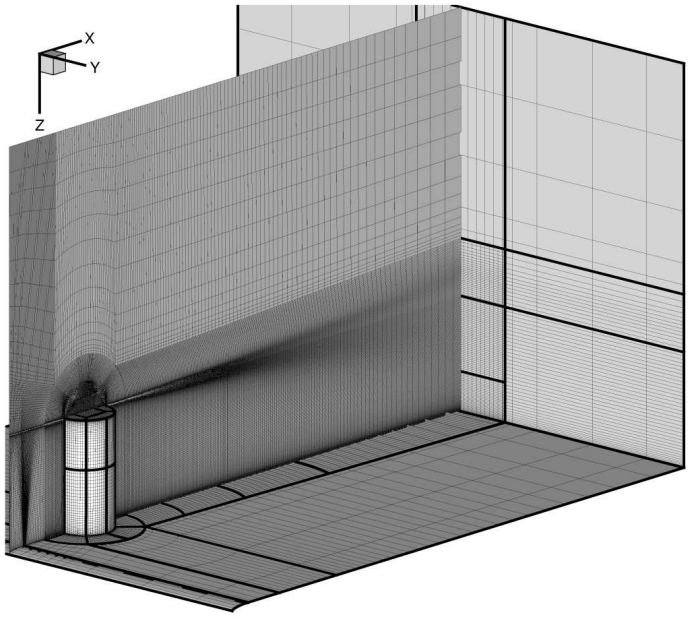

Figure 2: Block-structured discretisation with 12.3 million grid points (walls and outflow show only every third grid line).

The results of initial simulations on a coarse grid have been combined with the spatial discretisation of the LES capable grid to determine that the temporal discretisation to be used for this grid should be lower than $0.00555D/U_\infty$. The chosen time step size of $\Delta t = 0.005D/U_\infty$ ensures that no cell is traversed in a single time step. In physical units this time step corresponds to $\Delta t = 0.0000231\,\mathrm{s}$ and provides a sampling rate of approximately 43 kHz. Using this time step, a convective unit requires 200 time steps and the complete flow field is traversed in 2241 time steps based on the inflow velocity U_∞.

2.2 Boundary conditions

The present configuration is investigated experimentally in an open wind tunnel of the Göttingen type. Thus, slip conditions are applied to the upper and lateral boundaries, whereas no-slip conditions are applied to all physical walls. To ensure the non-reflective movement of arbitrary flow structures across the downstream boundary, a convective outflow condition $\frac{\partial \Phi}{\partial t} + U_m \frac{\partial \Phi}{\partial n} = 0$ is used, where U_m is the average outflow velocity to conserve the mass flux and n is the direction normal to the outflow boundary.

Due to the proximity of the inlet boundary and cylinder (distance is $1.375D$), a spatially-variable inflow profile is required taking into account the obstacle blockage. By extending the upstream region to $20D$, such a profile was obtained from a precursor simulation. Such extension of the upstream region would not be feasible in the full unsteady computation for reasons of numerical cost. A steady inflow profile has been imposed, which is considered acceptable due to the low turbulence intensity and the expected laminar regions on the cylinder front.

2.3 Large-Eddy Simulation

The Navier-Stokes equations for incompressible flows with the Cartesian coordinates x_i, the velocity components u_i, the pressure p, density ϱ and constant kinematic viscosity ν are given by the conservation of mass and momentum.

$$\begin{aligned} \frac{\partial u_i}{\partial x_i} &= 0 \\ \frac{\partial u_i}{\partial t} + \frac{\partial}{\partial x_j}(u_i u_j) &= -\frac{1}{\varrho}\frac{\partial p}{\partial x_i} + \nu \frac{\partial^2 u_i}{\partial x_j x_j} \end{aligned} \tag{1}$$

In the case of Large-Eddy Simulation these equations are filtered in space, formally defined as the convolution of a function with a filtering kernel G, e.g.

$$\widetilde{u}_i(x_i) = \int_{-\infty}^{\infty} G(x_i - \xi_i)\, u_i \, \mathrm{d}\xi \tag{2}$$

such that

$$u_i = \widetilde{u}_i + u_i' \tag{3}$$

results, with the resolvable scale part $\widetilde{u}_i$ and the subgrid scale part u_i'. By substituting the decomposition in equation (3) for the velocity u_i and pressure p and filtering, the LES equations with the filtered quantities are obtained.

$$\begin{aligned} \frac{\partial \widetilde{u}_i}{\partial x_i} &= 0 \\ \frac{\partial \widetilde{u}_i}{\partial t} + \frac{\partial}{\partial x_j}(\widetilde{u}_i \widetilde{u}_j) &= -\frac{1}{\varrho}\frac{\partial \widetilde{p}}{\partial x_i} + \nu \frac{\partial^2 \widetilde{u}_i}{\partial x_j x_j} - \frac{\partial \tau_{ij}}{\partial x_j} \end{aligned} \tag{4}$$

Unfortunately, the filtering of the nonlinear convective terms in the momentum balance leads to additional terms, which are referred to as the subgrid stresses $\tau_{ij} = \widetilde{u_i u_j} - \widetilde{u}_i \widetilde{u}_j$ and must be modelled. The subgrid scale (SGS) model is designed to account for the turbulent scales not resolved by the grid and the discretisation scheme. In the present work, the standard Smagorinsky (1963) model is applied without any wall modelling.

$$\tau_{ij} = -2\nu_{sgs}\widetilde{S}_{ij} \tag{5}$$

$$\widetilde{S}_{ij} = \frac{1}{2}\left(\frac{\partial \widetilde{u}_i}{\partial x_j} + \frac{\partial \widetilde{u}_j}{\partial x_i}\right) \tag{6}$$

Employing the Boussinesq hypothesis (5) with the subgrid scale viscosity ν_{sgs} and the strain rate tensor $\widetilde{S}$ for the resolved scales (6), this model simply derives ν_{sgs} for the unresolved scales from the filter width, which is set to the local grid size Δ obtained from the cell volume ΔV_{ijk}.

$$\nu_{sgs} = (C_s\Delta)^2\sqrt{2\widetilde{S}_{ij}\widetilde{S}_{ij}} = (C_s\Delta)^2\left|\widetilde{S}\right| \tag{7}$$

$$\Delta = \sqrt[3]{\Delta V_{ijk}} \tag{8}$$

The value of the model constant C_s is flow-dependent and is found to vary from 0.065 to 0.25 . For the simulation presented in this work the constant was set to $C_s = 0.1$.

2.4 Detached-Eddy Simulation

Detached-Eddy Simulation is a modification of a turbulence model used to close the unsteady Reynolds-averaged Navier-Stokes equations (U-RANS). The definition of the approach by Spalart *et al.* (1997) is introduced such that a non-zonal hybrid RANS-LES coupling is obtained.

The classical Reynolds-averaging of the Navier-Stokes equations (1) leads to the usual decomposition of the dependent variables into a time-averaged component $\overline{u}_i$ and a modelled fluctuation u_i'.

$$\overline{u}_i = \frac{1}{2T}\int_{-T}^{T} u_i(t)\,\mathrm{d}t \tag{9}$$

The extension of this approach to unsteady RANS means that a transient term is retained in $\overline{u}_i$ and that the dependent variables in the U-RANS equations (11) are now not only a function of space, but also a function of time. In this way, the decomposition of the field variables can be written as the sum of the time-averaged part $\langle\overline{u}_i\rangle$, the resolved fluctuation $\widetilde{u}_i$ and the modelled turbulent fluctuation u_i'.

$$u_i = \overline{u}_i + u_i' = \langle\overline{u}_i\rangle + \widetilde{u}_i + u_i' \tag{10}$$

$$\begin{aligned} \frac{\partial\overline{u}_i}{\partial x_i} &= 0 \\ \frac{\partial\overline{u}_i}{\partial t} + \frac{\partial}{\partial x_j}(\overline{u_i u_j}) &= -\frac{1}{\varrho}\frac{\partial\overline{p}}{\partial x_i} + \nu\frac{\partial^2\overline{u}_i}{\partial x_j x_j} - \frac{\partial\overline{u_i' u_j'}}{\partial x_j} \end{aligned} \tag{11}$$

Similar to deriving the LES equations, the time averaging of the Navier-Stokes equations leads to an additional term, which is the gradient of the Reynolds stress tensor $R_{ij} = \varrho\overline{u_i' u_j'}$. This term includes the turbulent fluctuations to be expressed in this work by a turbulence model.

By again using the Boussinesq hypothesis $\overline{u_i' u_j'} = -2\nu_t\overline{S}_{ij}$ the problem is reduced to one unknown proportionality factor ν_t obtained here from two parameters by the LLR k-ω turbulence model (Rung & Thiele, 1996). The model used introduces two additional equations for the turbulent kinetic energy k (13) and the turbulent frequency ω (14), written here in the incompressible form.

$$\nu_t = \tilde{c}_\mu\frac{k}{\omega} \tag{12}$$

$$\frac{\partial k}{\partial t} + \frac{\partial(k\overline{u}_i)}{\partial x_i} = P_k - \beta_k k\omega + \frac{\partial}{\partial x_i}\left[\left(\nu + \frac{\nu_t}{Pr_k}\right)\frac{\partial k}{\partial x_i}\right] \tag{13}$$

$$\frac{\partial\omega}{\partial t} + \frac{\partial(\omega\overline{u}_i)}{\partial x_i} = P_\omega - \beta_\omega\omega^2 + \frac{\partial}{\partial x_i}\left[\left(\nu + \frac{\nu_t}{Pr_\omega}\right)\frac{\partial\omega}{\partial x_i}\right] \tag{14}$$

The variables, coefficients and damping functions, summarised in Rung & Thiele (1996), are not relevant to the discussion, which focuses on the DES modification of this model. Following the DES practice, the turbulent length scale of the RANS turbulence model l_{RANS}, which is included indirectly in this model, is to be replaced by the length scale $l_{DES} = \min(l_{RANS}, C_{DES}\tilde{\Delta})$. The constant C_{DES} is obtained by calibration against decaying isotropic turbulence and the definition of the grid size $\tilde{\Delta} = \max(\Delta_x, \Delta_y, \Delta_z)$ is suitable for structured grids. In order to reduce the eddy viscosity ν_t the turbulent length scale $l_{RANS} = \frac{k^{3/2}}{\epsilon} = \frac{k^{1/2}}{\beta_k\omega}$ in the dissipation term $\epsilon = \beta_k k\omega$ of the transport equation for k (13) is replaced by the appropriate DES length scale (Bunge *et al.*, 2007).

$$\beta_k k\omega \quad \text{replaced by} \quad \frac{k^{3/2}}{\min(l_{RANS}, C_{DES}\tilde{\Delta})} \tag{15}$$

The DES modification of the URANS equations is combined with a hybrid convection scheme as proposed by (Travin *et al.*, 2002). The model constant was calibrated to $C_{DES} = 0.75$.

2.5 Evaluation of statistical quantities

In the first instance, the comparison of experimental and numerical results is based on statistical quantities (mean field, Reynolds stresses, triple correlations, etc.) evaluated from the unsteady field data. Apart from the simple averaging during a simulation, the summation of n-th order fluctuations with respect to the mean flow requires additional work, because the mean quantities are not known in advance.

In the present work statistical moments of first to third order are evaluated, including the Reynolds stresses as well as pressure-velocity correlations. For the computation of the Reynolds stresses, as an example of a double correlation, the decomposition of the velocity components (3, 10) is introduced to express the fluctuations by some available mean quantities.

$$\begin{aligned}\overline{u_i' u_j'} &= \overline{(u_i - \overline{u}_i)(u_j - \overline{u}_j)} \\ &= \overline{u_i u_j} - \overline{\overline{u}_i u_j} - \overline{u_i \overline{u}_j} + \overline{\overline{u}_i \overline{u}_j} \\ &= \overline{u_i u_j} - \overline{u}_i \overline{u}_j - \overline{u}_i \overline{u}_j + \overline{u}_i \overline{u}_j \\ &= \overline{u_i u_j} - \overline{u}_i \overline{u}_j\end{aligned} \tag{16}$$

The terms $\sum u_i u_j$ and $\sum u_i$ are summarised and stored together with the number of samples n during the simulation. In this way, the double correlations can be computed at the output stage and the simple enhancement of the statistical base is possible.

$$\overline{u_i' u_j'} = \frac{1}{n} \sum u_i u_j - \frac{1}{n} \sum u_i \frac{1}{n} \sum u_j \tag{17}$$

The same procedure has been extended for the computation of triple correlations, whose evaluation are of interest for Reynolds stress models (RSM) and the understanding of three-dimensional turbulent fluctuations.

$$\begin{aligned}\overline{u_i' u_j' u_k'} &= \overline{(u_i - \overline{u}_i)(u_j - \overline{u}_j)(u_k - \overline{u}_k)} \\ &= \overline{u_i u_j u_k} - \overline{\overline{u}_i u_j u_k} - \overline{u_i \overline{u}_j u_k} + \overline{\overline{u}_i \overline{u}_j u_k} - \overline{u_i u_j \overline{u}_k} + \overline{\overline{u}_i u_j \overline{u}_k} + \overline{u_i \overline{u}_j \overline{u}_k} - \overline{\overline{u}_i \overline{u}_j \overline{u}_k} \\ &= \overline{u_i u_j u_k} - \overline{u}_i \overline{u_j u_k} - \overline{u}_j \overline{u_i u_k} + \overline{u}_i \overline{u}_j \overline{u}_k - \overline{u}_k \overline{u_i u_j} + \overline{u}_i \overline{u}_j \overline{u}_k + \overline{u}_i \overline{u}_j \overline{u}_k - \overline{u}_i \overline{u}_j \overline{u}_k \\ &= \overline{u_i u_j u_k} - \overline{u}_i \overline{u_j u_k} - \overline{u}_j \overline{u_i u_k} - \overline{u}_k \overline{u_i u_j} + 2\,\overline{u}_i \overline{u}_j \overline{u}_k\end{aligned} \tag{18}$$

The computation of the triple correlations of the velocity fluctuations requires the summation of 10 additional terms $\sum u_i u_j u_k$, taking into account the symmetry and combinations of the different components.

The equations (4) and (11) reveal that the diffusive term consists of the viscous stresses and the modelled subgrid and turbulent Reynolds stresses respectively. Thus, these modelled stresses must be added to the statistics evaluated from the resolved scales. In the following these terms are neglected, because on the one hand their size is comparatively small in a well-resolved LES and on the other hand not all terms are accessible in the simulation. This problem becomes more evident by evaluating triple correlations for which modelled fluctuations (double correlations) would have to be separated and reassembled. However, the influence of the unresolved scales on the resolved scales is incorporated by the respective model.

3 Results and discussion

The following sections summarise results obtained by LES and DES, which are compared with each other and to experiments, whereby the focus is mainly on statistical flow quantities.

3.1 Flow topology

The structural classification of the unsteady flow pattern is very difficult, due to the tremendous number of small structures resulting from the high Reynolds number. Figure 3 shows instantaneous and time-averaged vortex structures of the LES and the time-averaged structures of the DES using the λ_2-criterion of Jeong & Hussain (1995). While the instantaneous snapshot (fig. 3a) reveals the unsteadiness of the flow, the time-averaged visualisations (fig. 3b-c) allow for the detection (in combination with a detailed analysis of the flow field) of the main flow features existing in the majority of the unsteady time-steps.

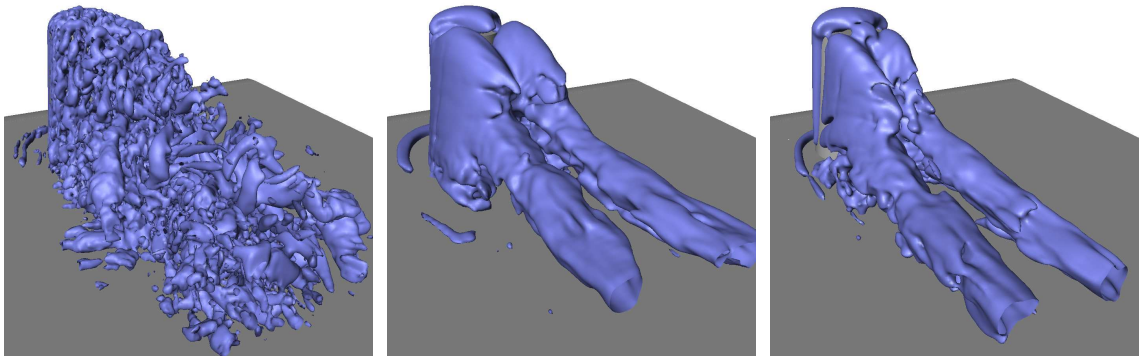

(a) LES, instantaneous snapshot. (b) LES, time-averaged. (c) DES, time-averaged.

Figure 3: Visualisation of predicted vortical structures (λ_2-isosurfaces).

Using the same grid and time step, both simulation approaches predict a system of vortices (Frederich *et al.*, 2007) of nearly identical topology, which is somewhat more pronounced in the lateral and streamwise directions in the LES. Beginning the classification at the cylinder top, the system of vortices consists of: counter-rotating recirculation vortices on the cylinder top reattaching on the top, side tip vortices, vortex shedding from the unstable shear layers of the sideways separation, a recirculation arch vortex at the downstream side of the cylinder, and a horse shoe vortex near the plate. These findings agree well with experimental measurements of Leder (2003) and Roh & Park (2003). While most investigations state coherent longitudinal vortex structures throughout the entire wake (Agui & Andreopoulus, 1992; Leder, 2003), the simulations reveal that the side tip vortices are merged into the tornado-like vortices formed by the recirculation downstream and the sideways vortex shedding. The trailing vortices farther downstream start near the reattachment on the plate and are induced by the impinging jet-like flow spreading and the relicts of the Kármán vortex shedding. In the regions between the side tip vortices and the trailing vortices, fluid from the surrounding flow is entrained and moved towards the plate and the symmetry plane. This rotational character of the movement is found by the λ_2-criterion (fig. 3b-c).

For infinite circular cylinders at $\mathrm{Re} = 200,000$, separation occurs at 80^o measured from the upstream side, and the transition occurs at nearly the same position (Zdravkovich, 1997). In both simulations, the separation line is bent downstream at the top of the cylinder, and is predicted by LES at about 80^o and much delayed by DES at around 100^o (fig. 4).

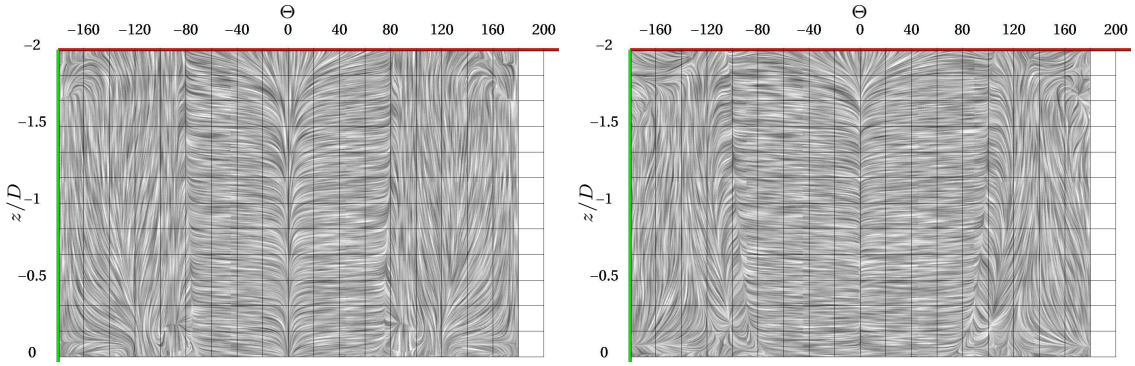

(a) LES, time-averaged (b) DES, time-averaged

Figure 4: Visualisation of surface streamlines on the cylinder shell using surface-LIC.

The DES encounters problems in the prediction of the correct separation position, because the RANS model, which is active near the wall, tends to produce eddy viscosity. This incorrectly produced eddy viscosity in the attached boundary layer causes a turbulent behaviour, and thus the separation occurs later, as would be the case at higher Reynolds numbers. This delayed separation in the DES results therefore leads to the reduced recirculation length and wake width visible in figure 3c.

3.2 Comparison to experiments

As summarised in the introduction, wall-mounted cylinders have been investigated experimentally with many combinations of aspect ratio and Reynolds number. The measurements of Kawamura *et al.* (1984) with various aspect ratios at $\mathrm{Re}_D = 32,000$ were concentrated on the near wall region of the cylinder. Recent results are available by Roh & Park (2003, $\mathrm{Re}_D = 148\,000$, $L/D = 1.25$) and by Pattenden *et al.* (2005, $\mathrm{Re}_D = 200,000$, $L/D = 1$) including flow visualisations, pressure and velocity measurements. The present numerical investigations were performed in close collaboration with experiments of the same configuration using LDA (Richter, 2005) and PIV measurements (Jensch *et al.*, 2006). All these experimental results are used here for quantitative comparison with the numerical results.

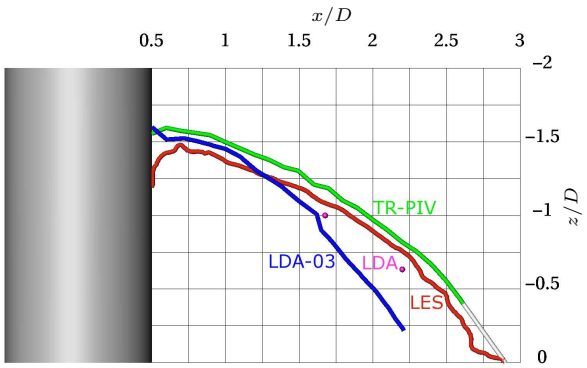

Figure 5: Time-averaged recirculation region ($\overline{u} = 0$) in the symmetry plane of LES compared with experiments of Leder (2003, LDA-03), Richter (2005, LDA) and Jensch *et al.* (2006, TR-PIV).

The experimental LDA and PIV results by Richter (2005) and Jensch *et al.* (2006) are used for extensive comparison with the numerical results. For this purpose the authors of these experiments provided the original datasets of their measurements. In the case of the LDA the time-averaged values were reproducible to an accuracy of 1% and 5% for the correlations. For the PIV measurements the uncertainty is in general slightly higher due to examination algorithms necessary for this imaging based method, but does not exceed 10%. The pressure distributions of Kawamura *et al.* (1984) and Pattenden *et al.* (2005) shown in figure 6 are extracted directly from the publications and could therefore include a maximum absolute deviation of 0.05.

In figure 5 LES results and recent experiments are compared in a representation of the recirculation region by a line of $\overline{u} = 0$ in the symmetry plane. The maximum deviation of this line between PIV as well as between the LDA points (two planes normal to the symmetry plane were measured) and LES is approximately $0.1D$. The tangential extrapolation of the PIV results to the ground plate shows a nearly perfect agreement of the reattachment point at $x/D = 2.88$. The LDA measurements of Leder (2003) were performed for a configuration with a reduced plate size.

The time-averaged pressure coefficient on half of the cylinder shell at $z/D = -1.0$ is shown in figure 6 as a function of the circumferential angle Θ. The comparison of the experimental curve by Kawamura *et al.* (1984) and the LES curve shows only minor differences concentrated in the sensitive separation region. Even though the experiments were performed at $\mathrm{Re}_D = 32,000$, the pressure coefficient for the subcritical turbulent flow regime at a cylinder is not a function of the Reynolds number. This finding is confirmed by the experiments of Pattenden *et al.* (2005), whose measured pressure distribution at $\mathrm{Re}_D = 200,000$ matches the results of Kawamura *et al.* (1984) in the same manner as the LES results do. The curve for the DES results predicts a supercritical flow regime with delayed separation explained previously. However, the various experimental and numerical results reveal that for the subcritical turbulent flow the pressure distribution at the central height of the cylinder is independent of the Reynolds number, but depends on the aspect ratio. All available experiments for $\mathrm{Re}_D = 200,000$ from the literature and some newer unpublished studies from a concurrent project detected a subcritical flow regime for the present boundary conditions.

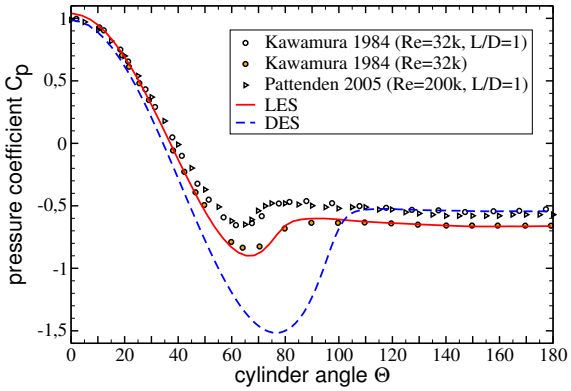

Figure 6: Pressure coefficient on the cylinder shell at $z/D = -1.0$ of LES and DES compared to experimental results by Kawamura *et al.* (1984) and Pattenden *et al.* (2005).

The time-averaged components of the velocity vector and the Reynolds stress tensor are compared qualitatively between LDA measurements and numerical results in a plane $x/D = 2.2$ at

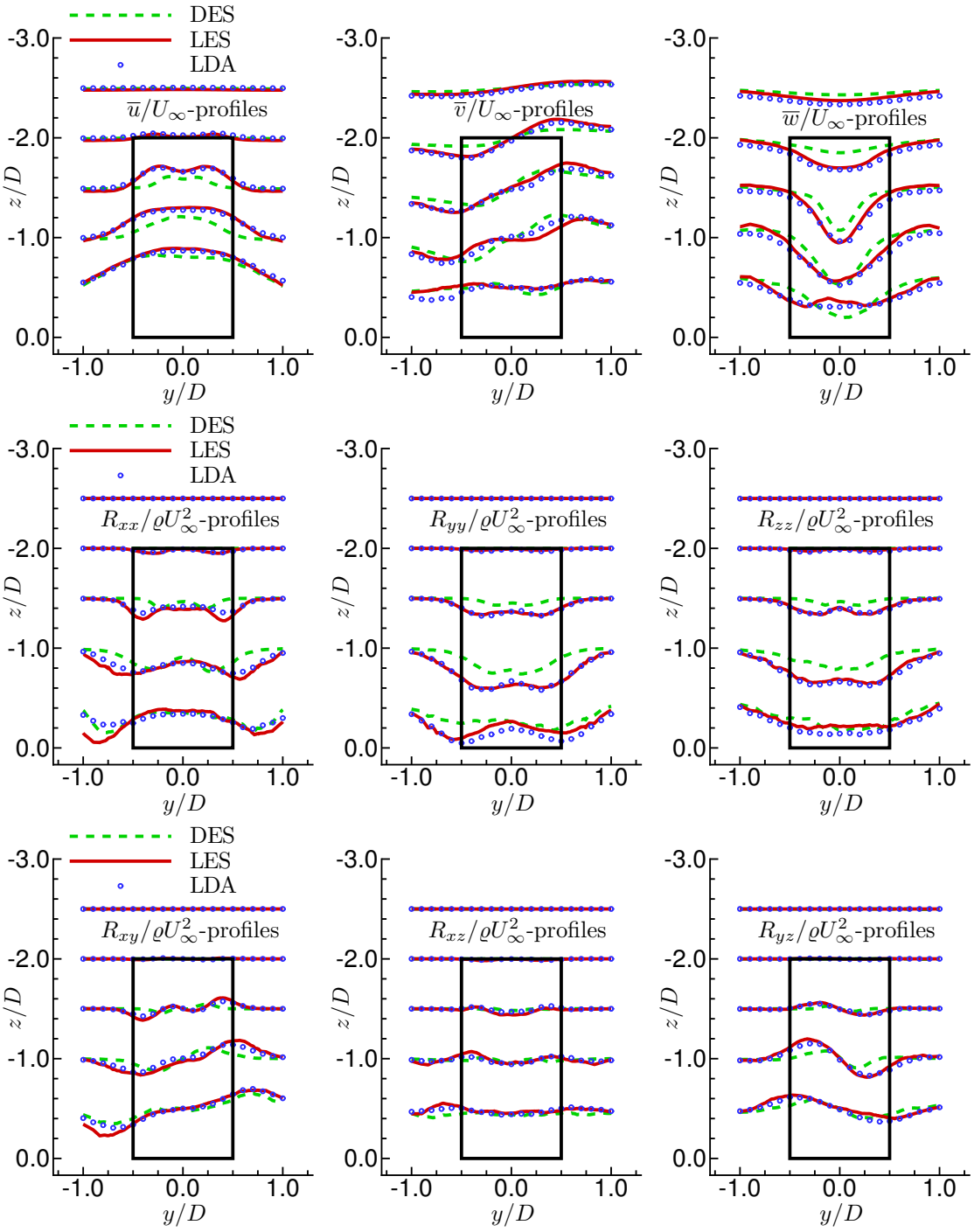

Figure 7: Time-averaged velocity and Reynolds stress components in the plane $x/D = 2.2$ compared between LDA measurements by RICHTER (2005) and numerical simulations.

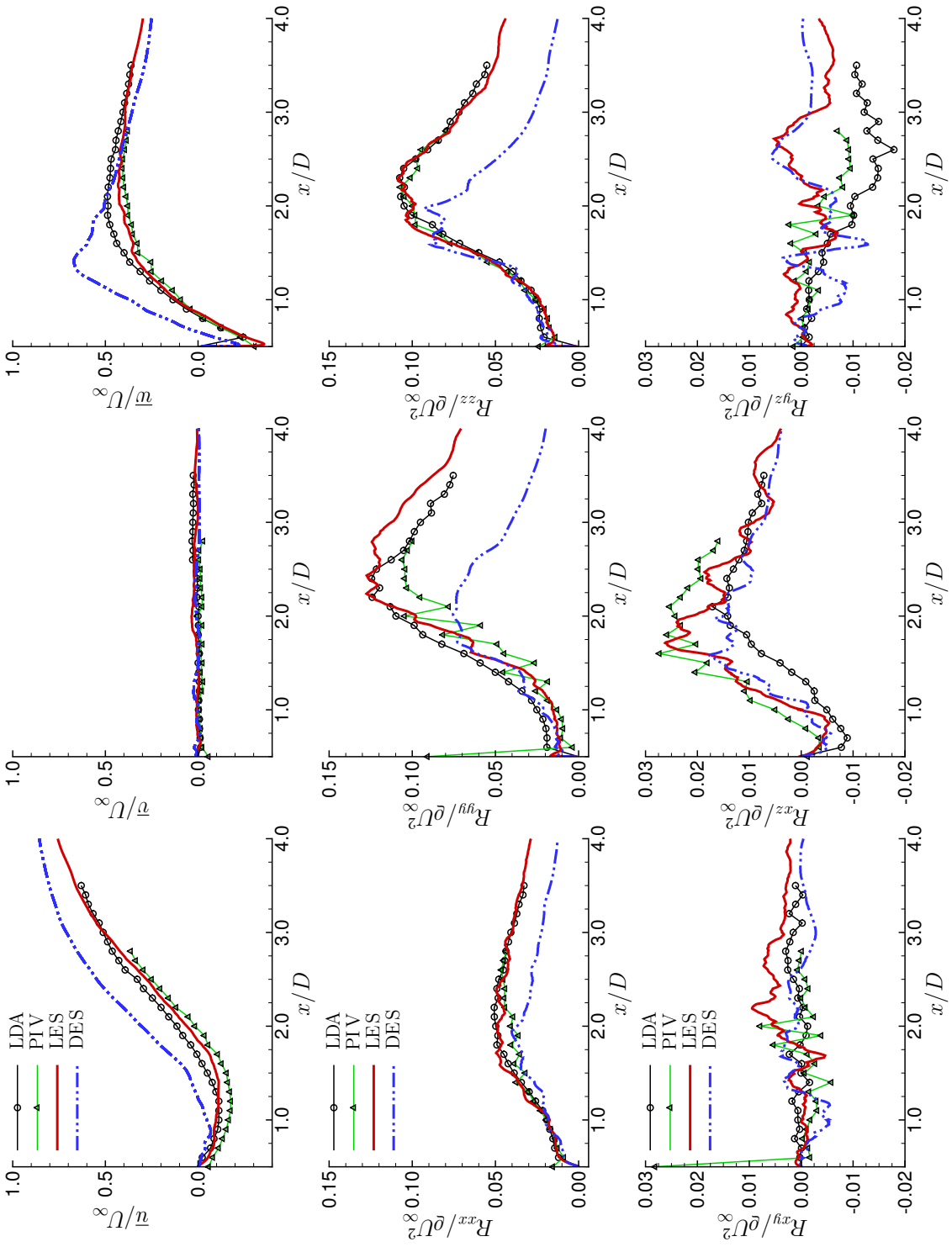

Figure 8: Time-averaged velocity and Reynolds stress components in the line ($y = 0$, $z/D = -1.0$) compared between LDA (Richter, 2005), PIV measurements (Jensch *et al.*, 2006) and numerical simulations.

discrete heights $z/D = -0.5, -1.0, ..., -2.5$, shown in figure 7. The different profiles show a very good agreement between LDA and LES, whereby the slight differences are believed to be due to an insufficient statistical base of the LES. The profiles of the DES show a larger disagreement compared to the experimental results because of the separation delay, but confirm the shape of the profiles qualitatively. However, the congruence of the LDA and LES profiles, especially for the second order moments, corroborate the successful work of both research groups.

The quantitative comparison of the time-averaged velocity and Reynolds stress components along a streamwise line in the wake with the LDA and time-averaged PIV measurements by Jensch *et al.* (2006) is depicted in figure 8. There is clearly very good agreement between the LES results and the experiment not only in the time-averaged velocity profiles but also in the turbulent fluctuations. The DES predicts at least a similar behaviour. The chosen line for comparison is a part of the symmetry plane, where no lateral mean flow components v should exist. Thus, the Reynolds stress components involving lateral velocity fluctuations v' require a much larger statistical base for convergence than the 30,000 time steps used. This insufficiency of all diagrammed data can be recognised in figure 8. In addition, the experimental data obtained by time-averaged PIV are intriguingly different to the LDA data, which is also visible in figure 5, although the same experimental setup was measured in either case.

3.3 LES versus DES

While the results presented above reveal insufficiencies of the DES due to problems with the treatment of the laminar-turbulent transition, a more detailed comparison between LES and DES will be given in this section.

The projected time-averaged velocity field of LES in two orthogonal planes is shown in figure 9 using the texture-based LIC (Line Integral Convolution) technique. The disagreement between LES and DES is shaded using a scalar measure of uncertainty defined by the magnitude of the difference velocity field $||\Delta\overline{U}|| = \sqrt{(\overline{u}_{LES,i} - \overline{u}_{DES,i})^2}$. This visualisation method has been proposed by Botchen *et al.* (2006), who also employed the numerical results of this work to demonstrate their concept. In this way, the images in figure 9 confirm at a single glance that the problems of DES arise only from the boundary layer treatment.

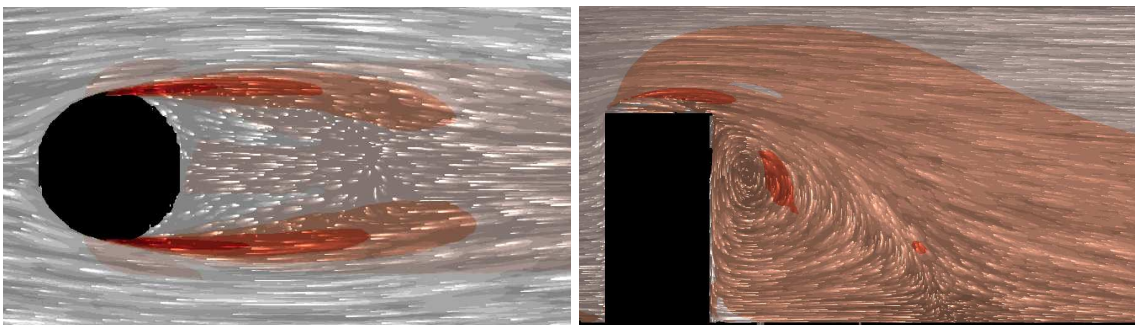

(a) plane $z/D = -1.01$ (b) plane $y/D = 0.01$

Figure 9: Line integral convolution of LES, shaded with the magnitude of the difference velocity field $||\Delta\overline{U}|| = \sqrt{(\overline{u}_{LES,i} - \overline{u}_{DES,i})^2}$ (red high; white towards zero).

Figure 10 a represents the temporal behaviour of the side force coefficient (integrated over all physical walls) for LES and DES over 50 convective units D/U_∞. The curve predicted by LES shows clearly an alternate vortex shedding of the separated flow, whereas this vortex shedding

is disturbed by other frequencies and the amplitude is reduced in the curve predicted by DES. The FFT (Fast Fourier Transformation) of these temporal signals in figure 10 b reveals that the associated Strouhal number $\mathrm{St} = fD/U_\infty$ for LES is 0.167 and for DES 0.160. These findings coincide with the experimentally determined Strouhal number of 0.162 (Jensch *et al.*, 2006) and numerically predicted value of 0.16 (Fröhlich & Rodi, 2003). Furthermore, the spectra of the side force coefficients identify a secondary frequency close to $\mathrm{St} = 0.2$ for the LES and at $\mathrm{St} = 0.21$ for the DES, which is typical for infinite cylinders at the present Reynolds number (Zdravkovich, 1997). This indicates a flow behaviour around the cylinder (near the plate) that is typical for infinite cylinders.

Table 2: Strouhal number and mean drag coefficient compared between various investigations and the present study.

authors	St	St_2	$\overline{C}_D$	Re_D	L/D	δ/D	BL [%]
Kawamura *et al.* (1984)	–	–	0.78	32,000	2	0.1	0.88
Okamoto & Sunabashiri (1992)	0.122[1]	–	0.73	47,000	2	0.1	1.3
Fröhlich & Rodi (2003)	0.16	–	0.88	43,000	2.5	0.1	7.3
Pattenden *et al.* (2005)	–	–	0.79[1]	200,000	1	0.1	4.2
Richter (2005)	0.162	–	–	200,000	2	0.042	6.8
Jensch *et al.* (2006)	0.162	0.20	–	200,000	2	0.042	6.8
present LES	0.167	0.20	0.82	200,000	2	0.06	2.85
present DES	0.160	0.21	0.55	200,000	2	0.04	2.85

[1] local value at $z/D = 0.5$

As Fröhlich & Rodi (2003) report, the drag is decreased when the aspect ratio is reduced due to the effect of the flow over the cylinder top, and the drag is increased with reduced boundary layer thickness δ/D. In addition a high blockage coefficient (BL) appears also to increase the drag, as the same authors note. Besides the comparison of Strouhal numbers the mean drag coefficient $\overline{C}_D$ of several investigations is also included in table 2. The drag coefficient of 0.82 predicted by LES is in very good agreement to the values taken from literature, especially considering the important parameters of influence mentioned above. Although the boundary layer thickness is over-predicted by LES but better by DES, the DES misses much of the pressure drag due to the delayed boundary layer separation. In the case of LES, it can be concluded that the tripping of the boundary layer on the plate did not work satisfactorily.

In addition to the spectral curves of the side force coefficient C_S, figure 10 b also includes the FFT spectra of the local pressure signal p at the point [2.4, 1.2, -1.0] for LES and DES. These two curves show that the wake fluctuates with fractions of both frequencies. Especially for LES, there is no clear separation of these frequencies in the spectrum of the side force coefficient, but the fraction of $\mathrm{St} = 0.167$ has a much higher amplitude. Since the Strouhal number of 0.2 can be attributed to the typical cylinder vortex shedding, the other frequency represents the combined effect of all dominant vortical structures (section 3.1).

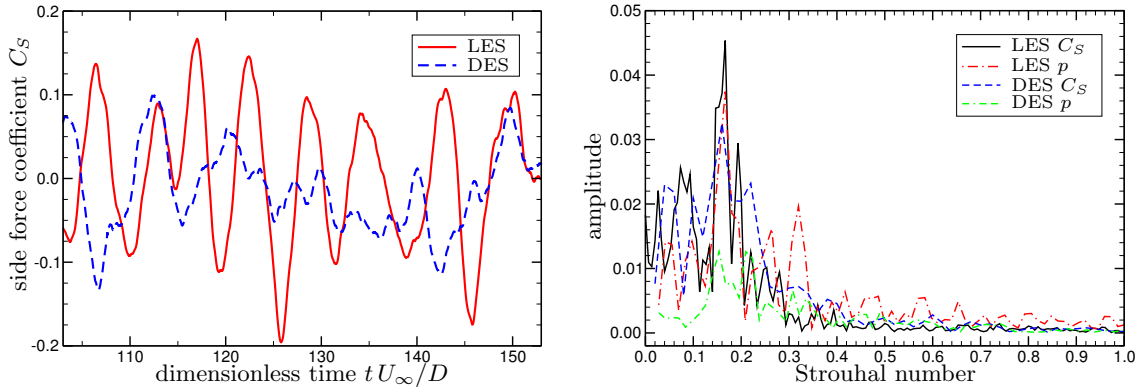

(a) side force coefficient

(b) FFT spectra

Figure 10: Global side force coefficients C_S and FFT of side force coefficients and local pressure signal p at [2.4, 1.2, -1.0] compared for LES and DES.

The detailed comparison of LES and DES reveals, that the difference between both approaches using the same numerical setup is limited to the incorrect boundary layer prediction of the DES. Thus, a DES in combination with an appropriate transition treatment should be able to predict qualitatively and quantitatively similar results to LES.

4 Conclusion and outlook

Large-Eddy Simulation and Detached-Eddy Simulation were performed for the turbulent separated flow around a wall-mounted finite cylinder. The numerical results reveal the capabilities of these approaches for predicting a flow, that is a marginal case between sub- and supercritical cylinder flow. While LES predicts the flow in very good agreement with experiments, the DES encounters problems in this comparison due to the turbulence production of the background RANS model in the boundary layer. The comparison presented includes statistical moments of higher order and with their good agreement to measurements the successful numerical prediction using LES is demonstrated.

The available results offer the potential to corroborate many more experimentally-obtained quantities for the whole flow field in the future, especially with respect to unsteadiness. The ongoing work and further research as well as further experiments using time-resolved PIV for this configuration at the University of Rostock will help to understand the unsteady flow patterns and to provide a combined database. Therefore, phase-averaging, POD, structure tracking and uncertainty visualisations will be applied to the numerical and experimental data.

Acknowledgement

The work presented is supported by the German Research Foundation (DFG) within the scope of the research project “Imaging based Measuring Methods for Flow Analysis” („Bildgebende Messverfahren für die Strömungsanalyse”). All simulations were performed on the IBM pSeries 690 supercomputer of the North German Cooperation for High-Performance Computing (HLRN). We thank both organisations cordially for their support. Special thanks go also to the experimental team at the University of Rostock for the provision of their data and to R. Botchen (VIS group, University of Stuttgart), who prepared the image in figure 9.

References

Agui, J. H., Andreopoulus, J. (1992) *Experimental investigation of a three-dimensional boundary-layer flow in the vicinity of an upright-wall mounted cylinder.* ASME Journal of Fluids Engineering 114:566–576.

Botchen, R.P., Weiskopf, D., Ertl, T. (2006) *Interactive visualization of uncertainty in flow fields using texture-based techniques.* In: *Electronic Proceedings International Symposium on Flow Visualization '06.*

Bunge, U., Mockett, C., Thiele, F. (2007) *Guidelines for implementing Detached-Eddy Simulation using different models.* Aerospace Science and Technology, 11:376–385.

Frederich, O., Wassen, E. Thiele, F., Jensch, M., Brede, M., Hüttmann, F., Leder, A. (2007) *Numerical simulation of the flow around a finite cylinder with ground plate in comparison to experimental measurements.* In: *Notes on Numerical Fluid Mechanics and Multidisciplinary Design*, 96:348–355, Springer.

Fröhlich, J., Rodi, W. (2003) *LES of the flow around a cylinder of finite height.* In: *Proc. of 3rd Int. Symp. on Turbulence and Shear Flow Phenomena*, Sendai, Japan.

Jensch, M., Brede, M., Richter, F., Leder, A. (2006) *Verwendung des Time-Resolved Stereo-PIV Messsystems zur Ermittlung zeitaufgelöster Geschwindigkeitsfelder im Nachlauf eines Kreiszylinders.* In: *Lasermethoden in der Strömungsmesstechnik*, PTB Braunschweig.

Jeong, J., Hussain, F. (1995) *On the identification of a vortex.* J Fluid Mechanics 285, 69–94.

Kawamura, T., Hiwada, M., Hibino, T., Mabuchi, I., Kumada, M. (1984) *Flow around a finite circular cylinder on a flat plate.* Bulletin of the JSME **27** (232), 2142–2151.

Krajnović, S. (2008) *Flow around a surface-mounted finite cylinder: a challenging case for LES.* In: *Notes on Numerical Fluid Mechanics and Multidisciplinary Design*, 97:305–315, Springer.

Krajnović, S., Davidson, L. (2004) *Large-eddy simulation of the flow around simplified car model.* SAE (Society of Automotive Engineers, Inc.), 2004-01-0227.

Leder, A. (2003) *3d-flow structures behind truncated circular cylinders.* In: Proc. of 4th ASME/JSME Joint Fluids Engin. Conf. Hawaii, USA, July, 2003, FEDSM2003-45083.

Okamoto, S., Sunabashiri, Y. (1992) *Vortex shedding from a circular cylinder of finite length placed on a ground plane.* ASME Journal of Fluids Engineering 114:512–521.

Pattenden, R.J., Turnock, S.R., Zhang, X. (2005) *Measurements of the flow over a low-aspect-ratio cylinder mounted on a ground plane.* Experiments in Fluids 39:10–21.

Pope, S.B. (2000) *Turbulent flows.* Cambridge University Press.

Rhie, C.M., Chow, W.L. (1983) *Numerical study of the turbulent flow past an airfoil with trailing edge separation.* AIAA Journal 21:1325–1332.

Richter, F. (2005) *Experimentelle Untersuchungen zur Charakterisierung der Strömungs- und Turbulenzstrukturen im Nachlauf eines Kreiszylinderstumpfes unter Berücksichtigung der Zentrifugalbeschleunigung.* PhD thesis, University of Rostock, Germany, ISBN 3-86582-167-7.

Roh, S.C., Park, S.O. (2003) *Vortical flow over the free end surface of a finite circular cylinder mounted on a flate plate.* Experiments in Fluids 34:63–67.

Rung, T., Thiele, F. (1996) *Computational modelling of complex boundary-layer flows.* Proc. 9th Int. Symp. on Transport Phenomena in Thermal-Fluid Engineering, Singapore.

Smagorinsky, J. (1963) *General circulation experiments with the primitive equations.* Monthly Weather Review 91:99–164.

Spalart, P.R., Jou, W.H., Strelets, M., Allmaras, S.R. (1997) *Comments on the feasibility of LES for wings and on a hybrid RANS/LES approach.* In: *Advances in DNS/LES, Proceedings of 1st AFOSR International Conference on DNS/LES*, pp. 137–147, Ruston, Greyden Press.

Travin, A., Shur, M., Strelets, M., Spalart, P.R. (2002) *Physical and numerical upgrades in the Detached-Eddy Simulation of complex turbulent flows.* In: *Fluid Mechanics and its Applications, Advances in LES of Complex Flows*, 65:239–254.

Xue, L. (1998) *Development of an efficient parallel solution algorithm for three-dimensional simulation of complex turbulent flows.* PhD thesis, ISTA, TU Berlin, Germany.

Zdravkovich, M.M. (1997) *Flow around circular cylinders.* Oxford University Press, New York.